Rotationally Inelastic Scattering of NO($A^2\Sigma^+$)+Ar: Differential cross sections and rotational angular momentum polarization

Supplemental Material for

'Rotationally Inelastic Scattering of NO($A^2\Sigma^+$)+Ar: Differential cross sections and rotational angular momentum polarization'

Thomas R. Sharples,[1] Thomas F. M. Luxford,[1] Dave Townsend,[1,2] Kenneth G. McKendrick[1] and Matthew. L. Costen[1,a]

[1]*Institute of Chemical Sciences, Heriot-Watt University, Edinburgh, EH14 4AS, U. K.*

[2]*Institute of Photonics & Quantum Sciences, Heriot-Watt University, Edinburgh, EH14 4AS, U. K.*

I. Ion Optics Design.

The final design of the ion optics is shown in Figure 1. In the following discussion, the eight electrodes are numbered from 1, the repeller plate, to 8, the final grounded electrode. The voltages applied to the electrodes are set so that the field gradient changes sharply at electrode 3, which may be considered the 'extractor' in the language of a Wiley-McLaren mass spectrometer. Electrodes 2 and 4 – 7 shield the interior of the ion optics from the effect of grounded components in the scattering chamber, and their voltages are set to smoothly vary the potential along the time-of-flight (TOF) axis.

The quality of focus provided by a VMI ion optic design is dependent on an ion's point of formation relative to a focal point in the source region of the electrode stack. For the design presented here, simulations indicate that the spread in arrival positions of a 4 mm diameter sphere of mono-energetic ions is equivalent to a velocity spread that varies between ±4.3 ms^{-1} and ±6.0 ms^{-1} for ions with an initial component of their velocity in the scattering plane of 2000 ms^{-1}, or stationary, respectively. This de-focussing spread is significantly smaller than the other fundamental sources of blurring, in particular the NO^+ recoil velocity arising from the ionization of the E-state with 532 nm is 8.5 ms^{-1}. This design therefore provides good focusing conditions over the volume and velocity range required for these experiments.

To discriminate against the pump-beam generated ions, the ion optics were designed to ensure optimal separation of the arrival times of ions of the same mass, generated at different times, so that gain-switching of the detector could be used to reject pump-generated ion signals. The two major potential contributions to the spread in ion arrival times are the spread in velocities and initial positions along the TOF axis. The spread in arrival times due to velocity was reduced by employing a relatively high extraction field, with the repeller plate set at 3kV, and using a long flight tube (79 cm between the source region and detector face), to allow the image to expand to a sufficient radius on the detector to give the required velocity

[a] Author to whom correspondence should be addressed. Electronic mail: m.l.costen@hw.ac.uk

resolution For SIMION simulations of a 4mm diameter sphere of ions with initial velocities of magnitude 840 ms^{-1}, the fastest recoil velocities attained by scattered NO(A) in these experiments, and an isotropic directional distribution, the spread of arrival times was 35 ns, providing a well-defined packet of ions at the detector in even this limiting case. The distance between electrodes 1 and 3, and between 3 and 8 were set to minimize the spread in arrival times due to formation of ions at different positions along the TOF axis. Simulations of an initially stationary 4 mm sphere of ions returned a negligible spread in arrival times of 0.7 ns. .As the delay between the pump and probe lasers is 400 ns, the ion packets produced by the pump-induced ionization and the scattered ions produced by the A-E probe ionization scheme are completely separated in time at the detector. In order to ensure the structural stability of the relatively large ion optics stack required for these experiments, they were supported by four stainless steel mounting rods. Insulation of the rods from the electrodes was achieved with a set of interlocking spacers between each electrode, which both set the spacing between the electrodes and acted as a sheath between the electrodes and their support rods. All insulating components in the ion optics stack were made from Semitron 225 (Quadrant Plastics) electrostatically dissipative plastic, to avoid build-up of static charges on these components leading to distortion of the images. Independent power supplies (Applied Kilovolts) were used to bias electrodes 1-3, as the quality of focus obtained by the ion optics was found to be very sensitive to the precise voltages applied to electrodes 2 and 3. A voltage divider network was used to step down the output of the power supply for electrode 3 to provide the bias voltages applied to electrodes 4-7.

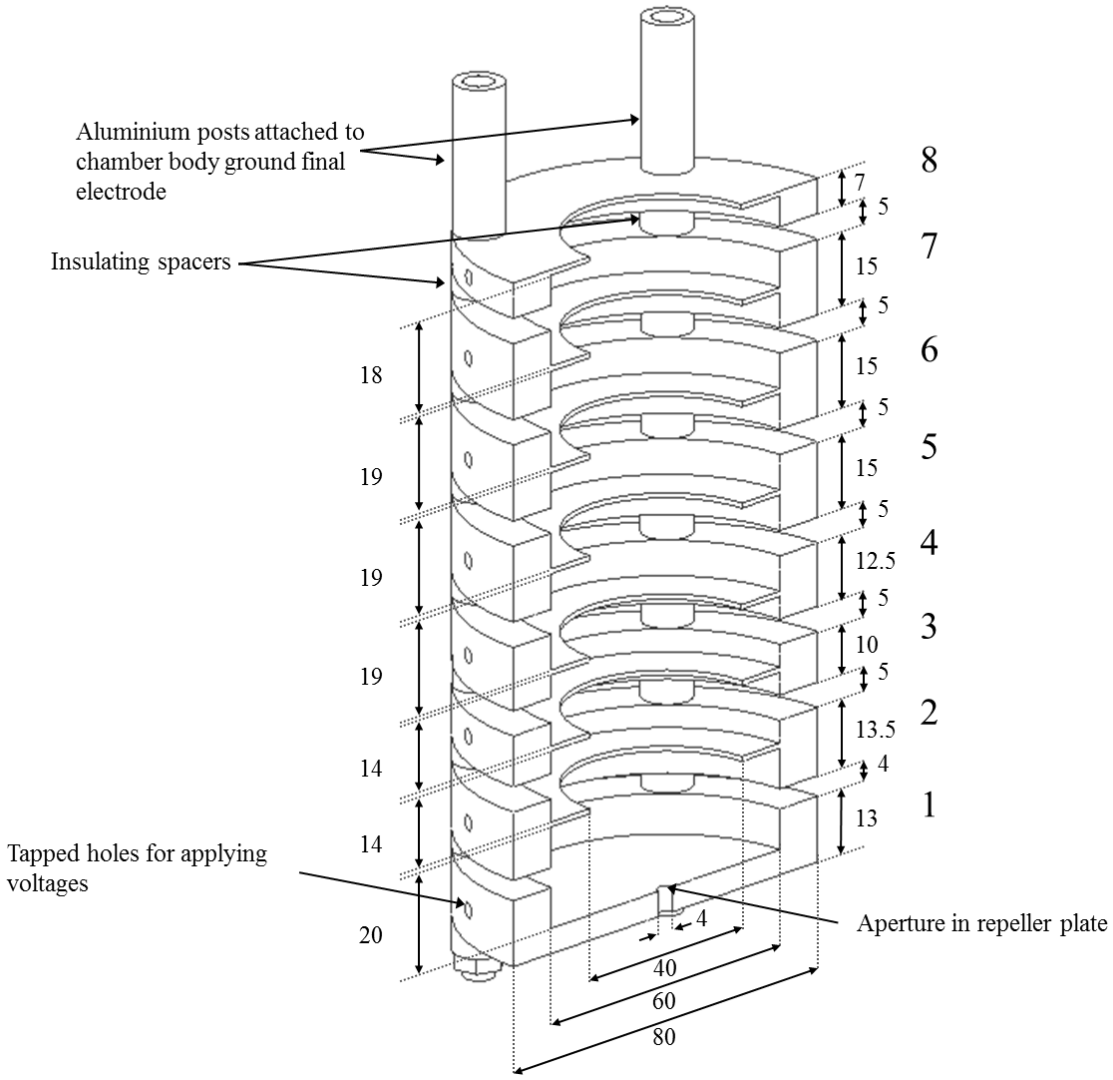

Figure 1: A schematic of the ion optics. Dimensions are given in millimetres. Each plate is labelled with a number 1 – 8, referred to in the text. The thickness of the central ring in electrodes 2 – 8 is 1 mm.

II. Determination of Zero Velocity Position and Determination of Molecular Beam Speed Distributions

As recently emphasized by von Zastrow et al., accurate determination of the position on the detector corresponding to zero laboratory frame velocity in the detector plane, as well as the mean velocities of the colliding species and their distributions, is essential in ensuring that differential cross sections and other angular features of the scattering are correctly extracted from images.[1]

The camera pixel corresponding to zero laboratory frame velocity in the plane of the image was determined as follows. NO was seeded separately (at 10% concentration) in He, Ne and Ar. These gas mixtures were each expanded through both

pulsed valves simultaneously. The NO($X^2\Pi$) in the two molecular beams was ionised in a (1+1) REMPI process via the $Q_1(0.5)$ transition of the A-X (0,0) band near 226 nm. The velocity-map images thus generated contain beam spots lying along axes corresponding to the direction of travel of each beam, with each gas mix providing a different mean speed. The mean velocities for each beam were obtained by fitting 2D Gaussian distributions to the images, and the camera pixel corresponding to zero velocity was determined from the intersection of straight line extrapolations through the 3 points along each axis. No detectable change in the position of zero velocity was detected during the course of a working day. These measurements were repeated each day, and the zero-position was found to be stable to within 1-2 pixels in each (*x*, *y*) image axis over a 4-week period. Figure 2 shows the sum of images acquired using each of the three NO/Rg mixtures. The axes corresponding to the directions of travel of the two molecular beams and their crossing point at zero velocity are indicated.

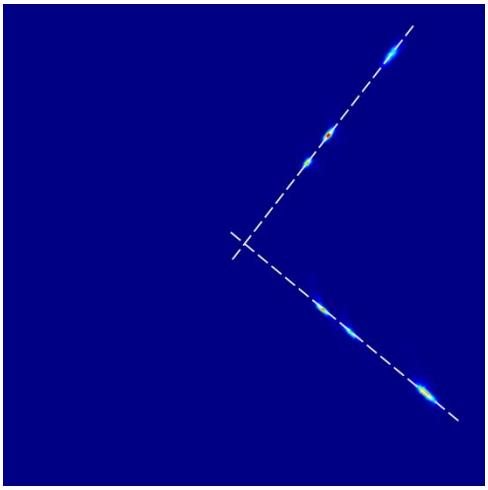

Figure 2. Sum of images for 10% NO seeded in He, Ne and Ar, respectively. The axes corresponding to the direction of travel of the two molecular beams are indicated by the dotted lines; their point of intersection determines the camera pixel that corresponds to zero laboratory frame velocity in the plane of the image.

Accurate determination of the mean velocities of the molecular beams and the form of their velocity distribution is critical to the image simulations used in data analysis, and the generation of collision energy averaged quantum scattering calculations. While images of NO in the molecular beams such as those discussed above may be used to determine the mean speeds of the colliders, the measurement of the velocity distribution in the beams is complicated by the finite velocity resolution introduced by a variety of processes, including ion-recoil (12.5 ms^{-1} for 226+226 nm ionisation), the finite velocity resolution of the ion optics, and the finite velocity resolution of the camera under these experimental conditions, 8.6 ms^{-1} per pixel, and the intensity distribution of each individual ion strike across multiple pixels.

For this reason, these distributions have been characterized in a separate set of experiments, in which NO molecules were 'tagged' at the crossing point of the two molecular beams, and their time-of-flight (TOF) to a second point recorded. A pulsed dye laser was used to excite NO(X) in the molecular beam to NO($A^2\Sigma^+$, v = 0) *via* the $R_1(0.5)+Q_{21}(0.5)$ transitions of the $A^2\Sigma^+$-$X^2\Pi$ (0,0) band. The excited NO(A, v = 0) molecules subsequently fluoresced back to the NO(X) ground state, with the (0,1) band having the largest Franck-Condon factor.[2] This provides a population in NO(X; v = 1) created at a known location and time, 'tagging' them. The tagged molecules were then separately probed 192 mm further along the molecular beam axis. A second pulsed dye laser was used to probe the $R_1(0.5)+Q_{21}(0.5)$ transitions of the A-X (1,1) band *via* laser induced fluorescence. The fluorescence lifetime of NO(A) is sufficiently short (≈ 200 ns) that the excitation and fluorescence processes may be considered to be instantaneous compared to the hundreds of microseconds between tagging and detection. The TOF distribution can therefore be straightforwardly measured by varying the delay between the lasers, and then converted to a velocity distribution using the known distance travelled. As expected, no NO(X, v = 1) was observed without tagging. An example velocity distribution is shown in Fig. 3, together with a fit to a Gaussian function. The excellent quality of the fit supports our decision to use Gaussian functions to model the molecular beam speed distributions in the analysis code and QS calculations. The fit in Fig. 3 resulted in a mean speed of 599 ± 3 ms^{-1} with a full width half maximum (FWHM) of 56 ± 3 ms^{-1}. The mean speeds and FWHM were determined for He, Ne and Ar carrier gases with a wide range of NO mixing ratios, as a function of the pulsed valve backing pressure. The properties of 1% NO/Rg mixes were taken to be representative of the velocity distributions in the pure rare gas beams.

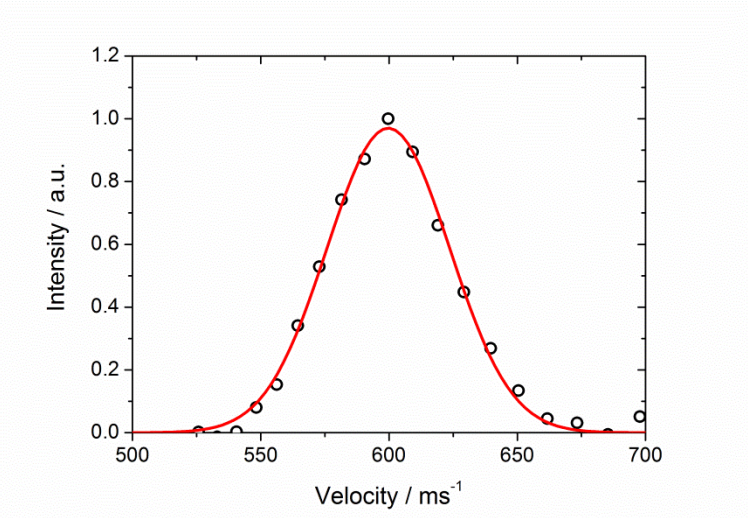

Figure 3: Measured velocity distribution (open circles) and fit to a Gaussian function (solid line) for NO in Ar at 10 % concentration.

III. Experimental Sources of Ion Image Blurring

As discussed in the main text, in simulating VMI images of crossed molecular beam scattering experiments, it is necessary to account for a number of aspects of the experiment which lead to blurring of the image, in the sense that the apparent distribution of velocities in the image is distorted from that of the true laboratory frame velocity distribution following scattering. The three most significant sources of blurring are the recoil experienced by the NO on ionization, the distribution of pixel intensity for each ion strike and the imperfect velocity focussing of the ion optics.

These effects are dealt with in the image simulation code by adding a velocity $\mathbf{v}_{\mathbf{exp}}$ to each lab frame velocity to give a velocity at which the ion was detected. This velocity is the sum of two contributions drawn from separate distributions. The first accounts for the impact of NO^+ recoil and is drawn from a spherically isotropic distribution of velocities with magnitude 8.6 ms^{-1}, the recoil experienced by NO on ionization from the $E^2\Sigma^+$ state through absorption of a 532 nm photon. The second velocity is drawn from a 2D Gaussian distribution of velocities lying in the plane of the detector, used to model the combined effects of the distribution over multiple pixels of each individual ion strike and imperfect velocity focussing. The FWHM appropriate for this blurring function was determined from images of the beam spot arising from NO in the molecular beam. The width of the beam spot perpendicular to the direction of travel of the beam is dominated by the effects of these blurring features due to the low angular divergence of the molecular beams. A FWHM of 30 ms^{-1} determined using this method was found to give simulated scattering images which agreed well with the finite resolution of the experimental scattering images.

IV. Derivation of the alignment moment distributions from the Kinematic Apse Model

Within the Kinematic Apse (KA) model, the projection of the angular momentum along the kinematic apse is conserved during the collision. Under these conditions, it is straightforward to predict the scattering angle dependence of the product rotational alignment. Our initial state, $N = 0$, is unpolarised by definition, with all population residing in the sole $m_N = 0$ sub-state. In the KA-frame, conservation requires that the product states N' must also have an angular momentum distribution in which only the $m_{N'} = 0$ sub-state is populated. Under these conditions the KA-frame product alignment moments must be;

$$A_0^{\{2\}}(KA) = -1 \qquad A_{+1}^{\{2\}}(KA) = 0 \qquad A_{2+}^{\{2\}}(KA) = 0 \tag{1a-c}$$

The alignment moments in the scattering-frame, $A_q^{\{K\}}(\theta)$, are related to the KA-frame moments by a frame-rotation.

$$A_q^{\{K\}}(\theta) = \sum_p d_{pq}^{(K)}(\beta) A_p^{\{K\}}(KA) \tag{2}$$

Here θ is the differential scattering angle, and β is the Euler angle that rotates the KA from into the scattering-frame. This Euler angle is the angle that the KA makes with the relative collision velocity, **k**, which is the Z-axis of the scattering-frame. The KA is defined in terms of the initial and final (**k'**) relative velocities as;

$$\hat{\mathbf{a}} = \frac{(\mathbf{k}' - \mathbf{k})}{|\mathbf{k}' - \mathbf{k}|} \tag{3}$$

Conservation of energy and linear momentum relate the magnitudes of **k** and **k'**, whilst θ is of course the angle between **k** and **k'**. The Euler angle, β, is therefore a different function of θ for each product rotational state.

Taking appropriate linear combinations to form the Hertel and Stoll renormalized alignment moments, and inserting Eqn. (1a)-1(c) into Eqn. (2) we find the following expressions for the scattering-frame alignment moments.

$$\begin{aligned} A_0^{\{2\}}(\theta) &= -P_2(\cos\beta) \\ A_{1+}^{\{2\}}(\theta) &= \sqrt{3}\sin\beta\cos\beta \\ A_{2+}^{\{2\}}(\theta) &= -\frac{\sqrt{3}}{2}\sin^2\beta \end{aligned} \tag{4a-c}$$

References

1. A. Zastrow, J. Onvlee, D. Parker, and S. van de Meerakker, EPJ Techniques and Instrumentation **2**, 11 (2015).
2. H. Scheingraber and C. R. Vidal, J Opt Soc Am B **2**, 343 (1985).
3. C. J. Eyles, M. Brouard, H. Chadwick, B. Hornung, B. Nichols, C. H. Yang, J. Kłos, F. J. Aoiz, A. Gijsbertsen, A. E. Wiskerke, and S. Stolte, Phys Chem Chem Phys **14**, 5403 (2012).
4. C. J. Eyles, M. Brouard, H. Chadwick, F. J. Aoiz, J. Kłos, A. Gijsbertsen, X. Zhang, and S. Stolte, Phys Chem Chem Phys **14**, 5420 (2012).
5. C. J. Eyles, M. Brouard, C. H. Yang, J. Kłos, F. J. Aoiz, A. Gijsbertsen, A. E. Wiskerke, and S. Stolte, Nat Chem **3**, 597 (2011).
6. A. Gijsbertsen, H. Linnartz, and S. Stolte, J Chem Phys **125**, 133112 (2006).
7. A. Gijsbertsen, H. Linnartz, G. Rus, A. E. Wiskerke, S. Stolte, D. W. Chandler, and J. Klos, J Chem Phys **123**, 224305 (2005).